applied sciences

MDPI

Article

Bionic Design of a Miniature Jumping Robot

Xianwei Bai [1,2], Deyi Kong [1,*], Qiong Wang [1,2], Xianhai Yu [3] and Xiaoxuan Xie [1,2]

[1] Hefei Institutes of Physical Science, Chinese Academy of Sciences, Hefei 230031, China
[2] Science Island Branch, Graduate School of University of Science and Technology of China, Hefei 230026, China
[3] School of Microelectronics, Hefei University of Technology, Hefei 230601, China
* Correspondence: kongdy@iim.ac.cn

Abstract: In response to the problem of low energy storage density in the structure of existing miniature jumping robots, this study designed a parallel single-degree-of-freedom double six-link jumping robot by imitating the physiological structure and jumping mechanism of wax cicadas. The designed six-link mechanism was first mathematically modeled, and to accommodate the jumping structure of this robot, a six-link mechanism with a smaller cam pushrod stroke was obtained by optimizing the linkage size and position parameters in the model. The dynamics of the robot's jumping process were then analyzed utilizing the second type of Lagrange equation to determine the joint angles of the robot's jumping phase. The results were compared with an ADAMS-based jumping simulation to verify the validity of the analysis of the dynamics. The feasibility of the structural design was then validated using ADAMS simulations. Finally, a physical prototype of the jumping robot was produced and tested; the findings revealed that the robot had good jumping performance, was stable in the air, fully discharged 600.2 mJ of energy, and was able to overcome obstacles measuring 220 mm in height and 330 mm in distance. The design of the jumping robot provides a novel approach to improving energy storage density and serves as a foundation for future research on footed jumping robots.

Keywords: imitation wax cicada; parallel single-degree-of-freedom double six-linkage mechanism; optimization; Lagrange equation; ADAMS

Citation: Bai, X.; Kong, D.; Wang, Q.; Yu, X.; Xie, X. Bionic Design of a Miniature Jumping Robot. *Appl. Sci.* **2023**, *13*, 4534. https://doi.org/10.3390/app13074534

Academic Editors: Qi Song and Qinglei Zhao

Received: 4 March 2023
Revised: 31 March 2023
Accepted: 1 April 2023
Published: 3 April 2023

1. Introduction

The rapid advancement of science and technology has necessitated the development of efficient, intelligent, and multifunctional micro-robots. Micro-robots are currently plagued by two main problems: the complex motions and long execution times of footed robots [1–3] traversing small target obstacles, and the restricted movement of wheeled tracked robots [4–6] with strong maneuverability in complex terrain. It becomes more difficult for micro-robots to navigate efficiently in natural unstructured environments as their size decreases [7]. Jumping robots are an excellent solution to these problems. With a small contact area and high energy efficiency, they can overcome obstacles several times their size [8,9] in a short period of time and adapt to unstructured terrain, which holds great potential for future applications in rescue and military operations and exploration.

In recent years, several research teams both domestically and abroad have developed some miniature jumping robots by drawing inspiration from insects including grasshoppers, fleas, and foam cicadas. Using two torsion springs as energy storage elements, the Swiss Federal Institute of Technology in Lausanne has designed a locust-like jumping robot with excellent jumping capabilities [10], which weighs only 7 g and is capable of jumping to a height of 1.38 m, which is about 27 times its own dimensional height. The Sant' Anna Institute of Higher Studies in Italy designed a cicada-like jumping robot with two linear springs for energy storage by optimizing the leg length ratio [11], which enables stable landings and continuous jumps with a jump height of approximately 100 mm. Based on

the principle of frog-leg jumping, Changlong Ye et al. from Shenyang University of Aeronautics and Astronautics designed a jumping robot with a deformed wheel structure that integrates wheeling and jumping [12], which can achieve jumping direction controllability, and tests have shown that a 300 g robot can achieve a maximum jump height of 285 mm. Riccy Kurniawan et al. from the University of Washington, U.S. proposed a Yak jumping robot [13]. The robot has a symmetrical mechanical structure with two shape memory alloy (SMA) spring actuators in the upper and lower parts, which are driven by radio transmission to store energy by converting the linear displacement of the SMA springs into a bending moment. According to the test results, the 216 mg robot has a vertical jump height of 138 mm, making it one of the top insect-grade wirelessly powered robots for jumping performance. The University of California proposed a crawling jumping robot driven by shape memory alloy actuators and aluminum foil [14] with magnet actuation to drive the whole system. The initial state of SMA has some pre-deformation, and jumping motion is promoted by induction heating of SMA and aluminum foil in a high-frequency alternating magnetic field. During the heating of the SMA berth, this design converts SMA from martensite to austenite. More elastic potential energy is stored, increasing the jump height, which is not found in conventional springs. A locust-like jumping robot developed by the Northwestern Polytechnic University in China mimicking the movements of the femur, tibia, and tarsus of the locust's hind legs [15] uses a linear spring to store energy and utilizes the negative rotation of the robot's body to counteract its tendency to flip in the air phase.

The aforementioned studies on miniature jumping robots have focused on the implementation and miniaturization of jumping functions but have neglected to design energy storage mechanisms with a greater energy storage density, the size of which directly affects the potential that a jumping robot can achieve. In this paper, the wax cicada, which has an excellent jumping ability, is used as a bionic prototype to design a jumping robot with a parallel single-degree-of-freedom six-link energy storage mechanism as the core, to solve the problem of insufficient energy storage in the existing energy storage mechanism of micro-robots and to provide a reference for the improvement of the energy storage density of future footed robots.

2. Design of the Wax-like Cicada Jumping Mechanism

2.1. Study of the Structure and Jumping Mechanism of the Hind Legs of a Bionic Prototype Wax Cicada

The wax cicada is an insect belonging to the family Cicadidae of the order Hemiptera, as shown in Figure 1a, its accustomed jumping movement pattern allows it to swiftly escape from threats posed by the outside world. Studies on wax cicadas have shown the presence of paired pleural arch structures on the hind thorax [16] that function as energy stores and contain a large number of tendon and arthroplasty elastic elements. It is this unique pleural arch that contributes the vast majority of the jumping energy source, as shown in Figure 1b [16].

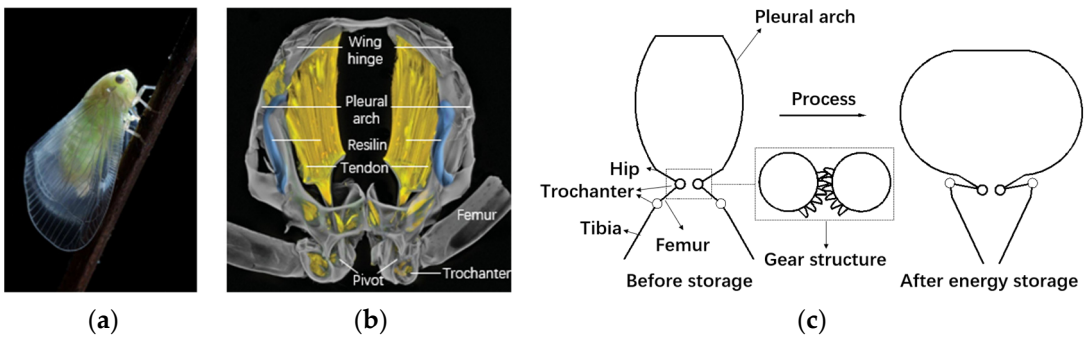

(**a**) (**b**) (**c**)

Figure 1. (**a**) Wax cicada in life; (**b**) Biological structure of the pleural arch [16]; (**c**) Simplified model of the jumping process.

Figure 1c shows a significant change in the posture of the hind legs of the wax cicada during the jump. Before energy storage, the angle between the femoral and tibial joints is in a large state. During energy accumulation, the elastic element contracts heavily to flex the pleural arch [17] and store large amounts of energy. The wax cicada has a cogwheel structure at the hip rotor and the released energy is transferred from the hip rotor to the end of the hindfoot. At the same time, the femoral and tibial joint stance gradually becomes smaller and reduces to a post-energy accumulation stance in which the wax cicada enters a pre-jump state, after which both feet are rapidly and synchronously extended due to the cogwheel structure at the hip rotor [18], producing a fast and powerful jump. The energy storage capacity of the pleural arch, which contains many elastic elements, is undoubtedly much higher than that of a single elastic element, and studies have shown that the jumping speed of the wax cicada is a staggering 5.5 m/s [19] compared to that of a flea with a jumping speed of 1 m/s [20].

2.2. Modeling of the Wax Cicada Jumping Mechanism

Based on the physiological structure and jumping mechanism of the wax cicada, the femur was used to simulate the wax cicada's femoral joint, the tibia to simulate the cicada's tibial joint, and two four-bar mechanisms consisting of two semi-pleural arch structures to simulate the cicada's two posterior pleural arch structures, respectively, and two linear springs were used to replace tendons and other elements to design the bionic energy storage structure model, as shown in Figure 2. In Figure 2, the connecting rods are articulated and the degree of freedom of the jumping leg mechanism is calculated as shown in Equation (1):

$$F = 3n - 2p_l - p_h = 3 \times 6 - 2 \times 8 - 1 = 1 \quad (1)$$

where n represents the number of moving parts and has a value of 6; p_l represents the number of low pairs in the kinematic pair and has the value of 8; and p_h represents the number of higher pairs in the kinematic pair and has the value of 1. The structure stores energy with the cam rotating counterclockwise as the prime mover, making contact with the rod CE and generating a collision force. As the mechanism only has one degree of freedom, the two rotating joints E and F of the four-rod mechanism will move in the curved slots, gradually changing the attitude of the four-rod mechanism, the four linear springs fixed in the two four-bar mechanisms will be stretched, and the two parallel six-link mechanisms will have a defined motion.

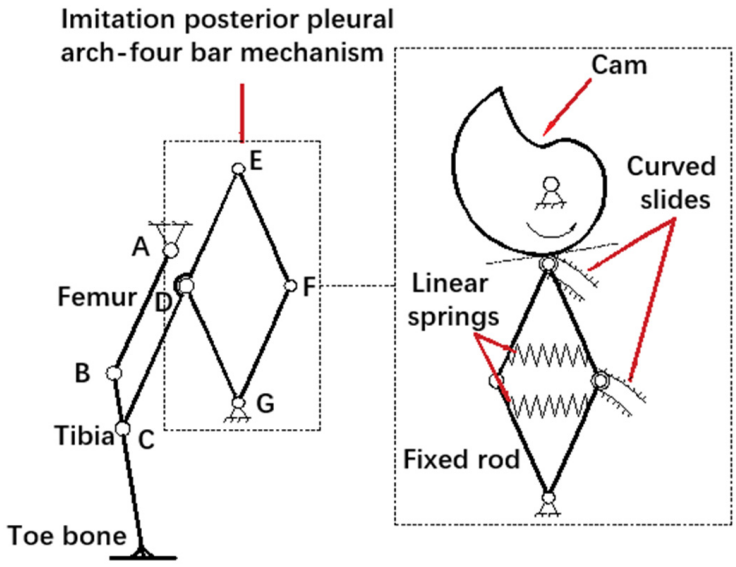

Figure 2. Structural diagram of the single six-link jump mechanism model.

2.3. Modeling of the Wax Cicada Jumping Mechanism

Based on the structural diagram of the jumping mechanism established above, a virtual prototype of the bouncing robot was created, as shown in Figure 3a. The robot is composed of four main parts: the front legs, the parallel double six-link mechanism, the body, and the energy control mechanism, which is shown in Figure 3b. The front legs of the robot provide support and attitude adjustment, the double six-link mechanism with four linear springs provides the power source for bouncing, the energy control mechanism stores and releases energy for the whole system, and the body part of the bouncing robot connects and balances the entire robot. In addition, the body is equipped with a servo control board to control the energy storage and release state of the entire system, as well as a battery that powers the entire robot.

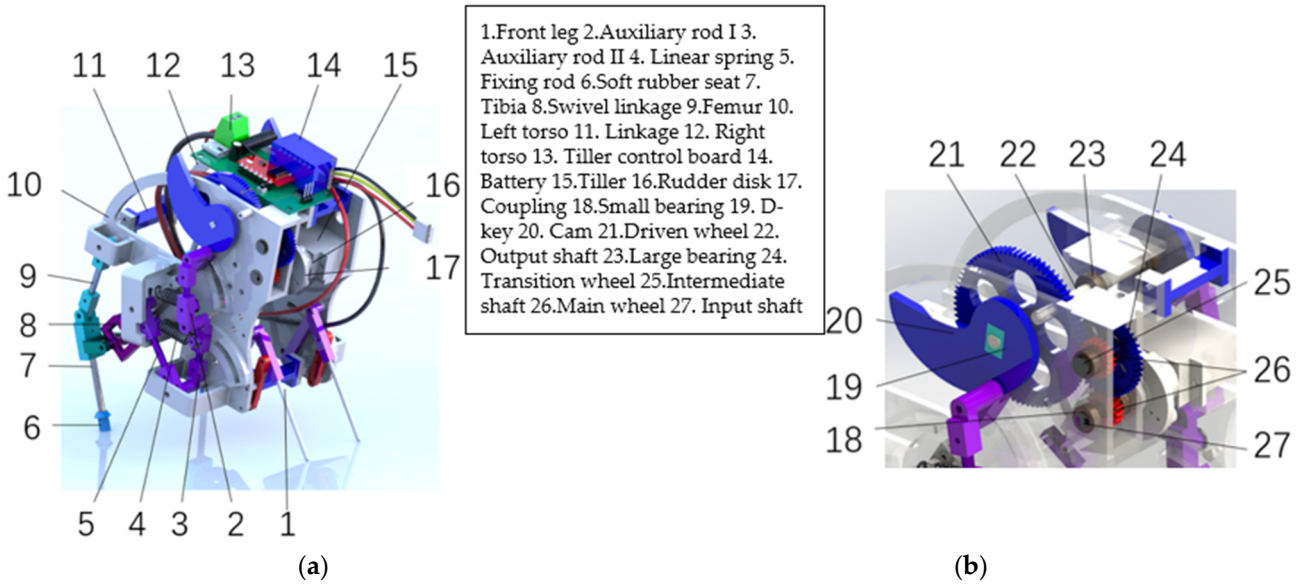

(**a**) (**b**)

Figure 3. (**a**) Overall structure of the bouncing robot; (**b**) Energy control structures for robots.

The robot bouncing principle is as follows: During the energy storage phase of the robot, the driving rudder rotates clockwise to transmit power through the rudder disk and coupling to the input shaft in a predetermined ratio, and then to the two cams of the output shaft via the energy control mechanism. The two cams rotate counterclockwise until they collide with the rotating linkage of the sub-mechanism (a four-bar mechanism), resulting in a collision force that forces two of the rotating joints to make a circular motion. The femur and tibia undergo a specific regular attitude change with the movement of the four-bar mechanism. At the same time, the four linear springs fixed to the two four-bar mechanisms are forced to stretch, and the whole system begins to store energy. The cam continues to rotate until it reaches the maximal energy storage for the whole system, at which point there are no more collision forces between the cam and the rotating joint, and the femur and tibia are in the ready-to-jump position. The cams continue to rotate after the energy is released, and the energy stored throughout the robot is instantaneously and completely released. The entire robot will return to its original stance in a very short time and the energy stored in the four linear springs will be instantly transferred through the entire mechanism to the toe bones causing the robot to jump by the reaction force of the ground on the toe bones.

2.4. Power Conversion Principle

A secondary reduction mechanism was employed in this study to reduce the speed and load inertia and multiply the torque on the output shaft to achieve the minimum torque required to stretch the four linear springs to their maximum. Figure 4 illustrates the

principle of how the servo amplifies the torque of the input shaft and reduces the speed of the input shaft to the output shaft. The process is as follows: The servo is coupled to the input shaft by a coupling and outputs with a torque of value τ_1, which is transmitted to the output shaft under the action of the reducer with a value τ_2. ω_1, ω_2 and ω_3 in the diagram represent the rotational speeds of the input, intermediate and output shafts, respectively. The theoretical variation of torque is related as:

$$\frac{\tau_2}{\tau_1} = \frac{Z_3}{Z_1} \cdot \frac{Z_2}{Z_1} = \frac{Z_3 \cdot Z_2}{Z_1^2} \tag{2}$$

In the above equation, Z_1, Z_2 and Z_3 correspond to the number of teeth on the driving gear, intermediate gear, and driven gear, respectively. Conversely, the theoretical relationship between the rotational speeds is expressed as follows:

$$\frac{\omega_3}{\omega_1} = \frac{Z_1^2}{Z_3 \cdot Z_2} \tag{3}$$

This multiplies the maximum torque of the output shaft and reduces the torque requirement of the rudder, while at the same time reducing the output shaft speed proportionally and increasing the overall energy storage time.

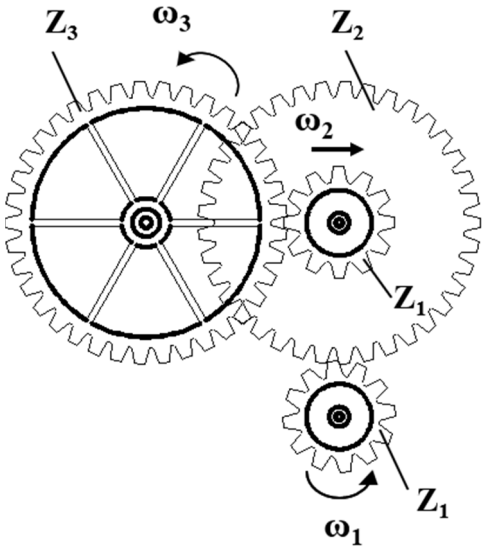

Figure 4. Power conversion diagram.

2.5. Bouncing Motion Process

The robot completing the entire bouncing motion is shown in Figure 5. To begin, the rudder control board drives the rudder to turn counterclockwise. The power from the rudder is transmitted via the energy control mechanism to the two cams on the output shaft, which are in contact with the two rotating links on the left and right, respectively, and the two six-link mechanisms in parallel begin to change stance in a synchronized manner. The four linear springs fixed to the four-bar mechanism are stretched, causing the robot's center of gravity to shift downwards gradually. At this point, the two cams continue to rotate, the attitude of the six-link mechanism changes, and the deformation of the linear spring gradually increases until the cams reach a critical point, at which point the robot's energy storage phase ends. During the release phase, the cams continue to rotate until they cross the critical point, at which moment the entire system instantly releases all its energy and the robot leaps up.

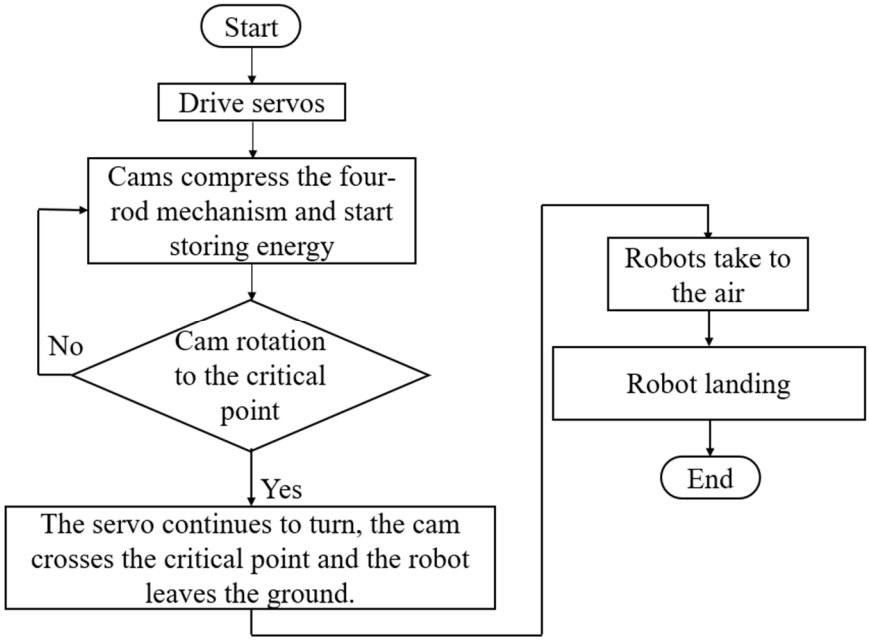

Figure 5. Bouncing movement flow chart.

3. Jumping Mechanism Analysis and Optimization

3.1. Design and Parameter Optimization of the Jumping Leg Mechanism

This section explores the effect of the angle of the variable C_1DG and the length of DG on the magnitude of the spring deformation, provided that the fixed rod DG and the length of DE are constants, to allow the double six-link mechanism to rotate to the limited position of maximum compression of the linear spring, as shown in Figure 6. To reduce the minimum torque required by the cam during compression, a cam with a small actuator stroke was first designed, followed by the calculation of the deformation of the spring when the rotating linkage is rotated clockwise to a critical state based on the profile of the cam, and the analysis of the variation law between the angle of the variable C_1DG and the length of DG and the deformation of the spring.

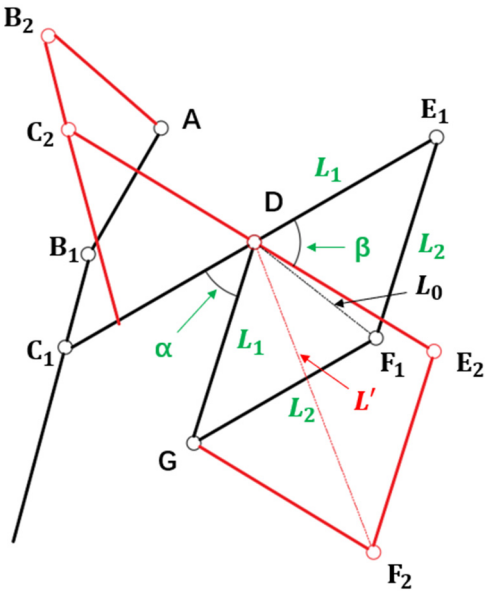

Figure 6. Mathematical model of a six-link mechanism.

In Figure 6, the six-rod mechanism $AB_1C_1DE_1F_1G$ represents the initial state of the jumping leg mechanism without energy storage, $AB_2C_2DE_2F_2G$ is the limit state of the jumping leg mechanism at maximum energy storage, the rotating linkage C_1E_1 rotates the fixed angle β to reach the critical state, and the DG rod is a fixed rod. According to the relationship between two linear spring positions with symmetry, $DE_1 = DG = L_1$ and is a constant, and $E_1F_1 = GF_1 = L_2$, L_2 is a variable. According to the given cam profile, $\beta = \pi/3$, let the initial length of the spring be L_0, the limit length at the maximum of the deformation variable is L', the angle between the rotating connecting rod C_1E_1 and the fixed rod DG is the variable α, and the value of α is in the range of $(0, \pi)$. In the triangle DE_1F_1, according to the cosine theorem, we have:

$$cos\frac{\pi-\alpha}{2} = \frac{L_1^2 + L_0^2 - L_2^2}{2L_0L_1} \tag{4}$$

In the triangle DE_2F_2:

$$cos\frac{\pi-\alpha-\frac{\pi}{3}}{2} = \frac{L_1^2 + L'^2 - L_2^2}{2L'L_1} \tag{5}$$

Simplifying the above two equations yields:

$$\begin{cases} L_0^2 - 2L_1 sin\frac{\alpha}{2}L_0 + L_1^2 - L_2^2 = 0 \\ L'^2 - 2L_1 cos\left(\frac{\pi}{3} - \frac{\alpha}{2}\right)L' + L_1^2 - L_2^2 = 0 \end{cases} \tag{6}$$

From Equation (6), it follows that:

$$L' - L_0 = L_1\left[\cos\left(\frac{\pi}{3} - \frac{\alpha}{2}\right) - sin\frac{\alpha}{2}\right] + \sqrt{L_1^2 cos^2\left(\frac{\alpha}{2} - \frac{\pi}{3}\right) - \left(L_1^2 - L_2^2\right)} - \sqrt{L_1^2 sin^2\frac{\alpha}{2} - \left(L_1^2 - L_2^2\right)} \tag{7}$$

In Equation (7), α and L_2 are two independent variables that have no influence on one another. Using the control variables method, the mathematical analysis of this function leads to the conclusion that the smaller the angle of α, the larger the value of $L' - L_0$, and the larger the deformation of the spring, while L_2 remains constant. If α remains constant, the value of $L' - L_0$ tends to increase as L_2 decreases. We thus propose a design principle that is compatible with this six-rod mechanism: the linkage length L_1 remains constant, the initial spring length L_0 and the limit length L' satisfy the conditions for the use of the spring, and the size of α or is L_2 is reduced in the six-rod mechanism so that the size of the linkage is reduced and the deformation of the spring is quickly maximized. There is, however, a theoretical minimum value for L_2, which is the minimum value when E_1F_1G coincides with the position of the dead point of the mechanism, when $E_1F_1G = 2L_2$.

3.2. Dynamical Modeling and Analysis

A common approach used for establishing the dynamic equation of robots is the Lagrange method. During the take-off phase of the robot, its joint angles can be obtained by solving the analytical equations. Assuming that the robot's tibia is in a state where it is not slipping on the ground and that the tibia and the ground can be regarded as a rotational connection, the generalized angle θ_1 between the tibia and the ground is used as the coordinate of the system; the dynamics of the robot in the take-off phase is modeled based on the Lagrange approach, as shown in Figure 7.

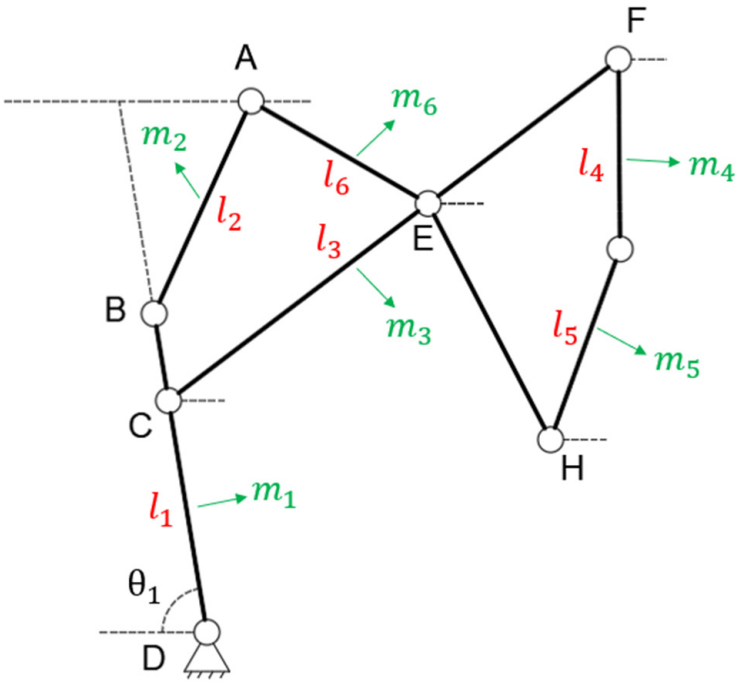

Figure 7. Overall dynamic model of the take-off phase.

In Figure 7, the point E is the center of mass of the body, m_i, l_i represent the mass and length of each bar, and the dynamic equation of the robot during the jumping phase is obtained by:

$$\begin{cases} \frac{d}{dt}\frac{\partial L}{\partial \dot{\Theta}_1} - \frac{\partial L}{\partial \Theta_1} = 0 \\ L = k - u \end{cases} \tag{8}$$

In the preceding equation, the dynamic energy k generated by each rod includes the linear velocity dynamic energy and angular velocity dynamic energy generated by the center of mass of that rod. Using the contact point between the tibia and the ground as the zero potential energy point, the potential energy u of the system can be divided into two parts, one part is the elastic potential energy of the spring and the other part is the total gravitational potential energy of the system composed of each rod, resulting in the dynamic energy and potential energy of the system when the robot jumps, as shown in Equation (9):

$$\begin{cases} k = \sum_{1}^{6} k_i = \frac{1}{4} m_i v_i^2 + I_i \omega_i^2 \\ u = 4 \bullet \frac{1}{2} k_c \Delta x^2 + 2 \sum_{1}^{6} m_i g h_i \end{cases} \tag{9}$$

In Equation (9), k_c is the spring's coefficient of elasticity, Δx is the spring deformation, g is the acceleration of gravity, v_i is the velocity of the center of mass of each linkage, h_i is the vertical coordinate of the center of mass of each linkage relative to the point of zero potential energy, and I_i is the rotational inertia of each linkage to the center of mass. Table 1 displays the parameters of the robot's connecting rods, such as mass, length, and inertia.

The dynamic equations were solved numerically using the Runge–Kutta method with an initial value of θ_1 of 88° and ω_1 of 0 rad/s. The final calculated output curves were compared with the simulation results in the ADAMS environment, as shown in Figure 8.

In Figure 8, the energy storage phase of the robot lasts from 0 to 5.02 s, during which the femur-tibia and tibia-ground angles gradually decrease, whereas the body-femur angle gradually increases. The curves of the body-femur, femur-tibia, and tibia-ground angles are approximately the same, indicating that there are minor errors between the simulation

results and the calculation results, but the curves are identical, demonstrating the validity of the dynamic analysis.

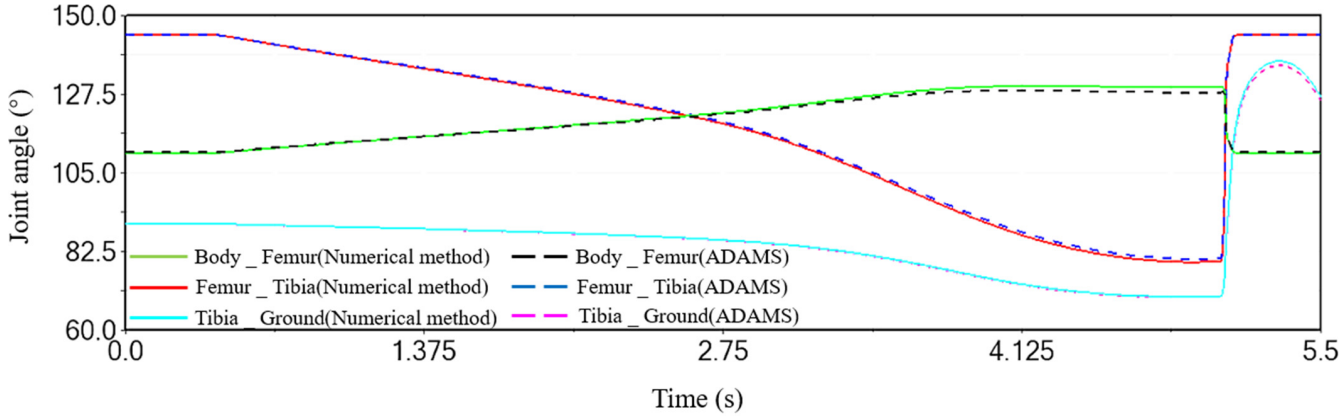

Figure 8. Joint angle during the take-off phase of the robot.

Table 1. Relevant parameters for robot components.

Components	Parts	Materials	Weight (g)	Length (mm)	Rotational Inertia (kg · mm^2)
Femur	-	Aluminum	1.4	36.8	0.63
Tibia	-	Aluminum	4.5	50.9	3.89
Rotary linkage	Connecting rod Connectors	Aluminum Photosensitive resin	5.6 0.4	75.5	2.85
Auxiliary rod I	Connectors Connecting rod	Photosensitive resin Aluminum	0.1 0.6	30.8	0.22
Auxiliary rod II	Connecting rod Connectors	Aluminum Nylon glass fiber	0.6 0.1	30.8	0.22
Body	Camshafts	Stainless steel	6	62	55.15
	Cams	Resin	4	-	
	Gear sets	Nylon glass fiber	6		
	Bearings	Steel	1.8		
	Servo		12		
	Steering wheel	Plastic	0.6		
	Couplings	Photosensitive resin	1.2	-	
	Forelegs	Nylon	5		
	Battery	-	16		
	Control panels	-	12		
	Other	-	75.4		
Total mass		-	166.6	-	-

4. ADAMS-Based Simulation Analysis of Bouncing Robot Motion

According to the structural design scheme of the imitation wax cicada jumping robot proposed in Section 2, the model was imported from SolidWorks into ADAMS for kinematic simulation analysis to predict the kinematic performance of the bouncing robot and to verify the feasibility of the overall mechanism design.

4.1. Component Type Parameters of the Bionic Bouncing Robot

Based on the 3D structure of the robot, a prototype model of the robot was assembled, of which the model parameters of the relevant components are shown in Table 2.

Table 2. Relevant component type parameters.

Components and Parameters	Numerical Values
Spring wire diameter ^ outside diameter ^ length (mm)	0.7 ^ 6 ^ 25
Modulus of active wheel ^ number of teeth (mm)	0.5 ^ 18
Modulus of intermediate wheel ^ number of teeth (mm)	0.5 ^ 42
Modulus of driven wheel ^ number of teeth (mm)	0.5 ^ 80
Small bearing bore ^ outer diameter ^ thickness (mm)	4 ^ 7 ^ 2.5
Large bearing bore ^ outer diameter ^ thickness (mm)	4 ^ 8 ^ 3
Servo mass (g) ^ max. torque (kg · cm)	12 ^ 5

4.2. Motion Simulation and Experiments

The process used for the simulation is as follows: according to the given material properties, add the material properties of each part in ADAMS, set the connection relationship between each part, add the collision force of the parts in contact, and finally add the driving force for simulation.

The trajectory of the robot's center-of-mass motion is determined from the simulation of the virtual prototype and is shown in Figure 9. It can be seen from the figure that the robot is relatively stable during its motion in the air, with no substantial overturning. At the end of the simulation, the bouncing performance data of the robot was obtained using the post-processing module of ADAMS, as shown in Figure 10a,b.

During the simulation, the robot saves energy from 0 to 5.02 s, the robot starts to store energy under the force of the cam, and the center of mass gradually drops to its lowest point. When the cam is ready to pass the contact boundary of the four-bar mechanism and the energy is about to be fully released, the system's energy storage achieves a maximum at t = 5.02 s. At t = 5.02~5.31 s, the robot releases energy, starts jumping, and gradually accelerates to the highest point with a jump angle of about 62°. The elastic potential energy accumulated in the robot during this process will be completely transformed into kinetic energy. The vertical height of the highest point is about 393 mm, and horizontal displacement will continue to increase until the robot hits the ground. When the robot begins to descend at t = 5.31~5.55 s, its gravitational potential energy at the highest point is completely converted into kinetic energy, and the robot lands at t = 5.55 s with a horizontal displacement of 595 mm, reaching the maximum. According to the center of mass displacement graph, the robot has a maximum bounce height of 306 mm and a maximum jump distance of 595 mm. The acceleration of the robot during the whole jumping process and the change of the torque of the rotating vice between the body and the femur and the femur and the tibia of the single six-link mechanism during the jumping process are shown in Figure 11a,b. During the gradual stretching of the linear spring and the energy storage process of the whole system, the center of gravity of the robot shifts downwards and has a smaller tendency of jumping up and down until 5.02 s and gains an instantaneous acceleration of a value of 275 m/s^2 during the jumping, after which the momentary acceleration changes to a gravitational acceleration of approximately 9.8 m/s^2. During the energy storage phase, the moment between the body and femur and femur and tibia in the six-link mechanism builds and then falls to zero at t = 5.02 s due to the immediate release of energy.

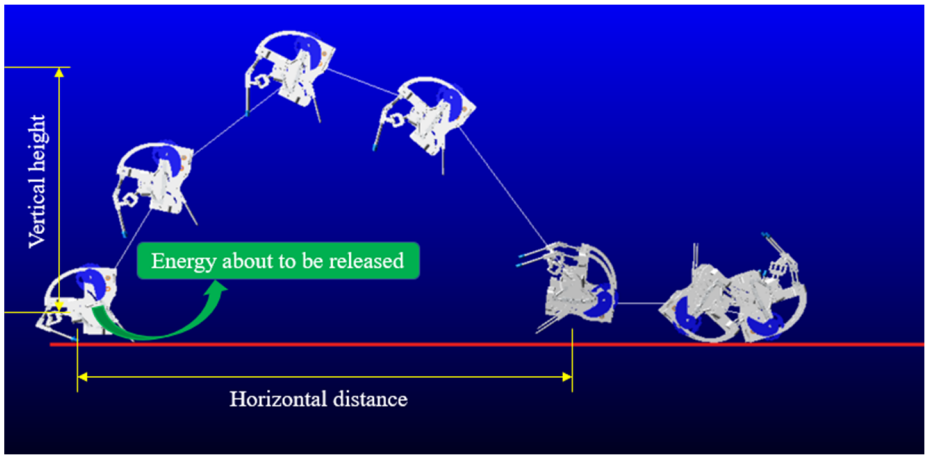

Figure 9. Movement diagram of a bouncing robot in a simulation environment.

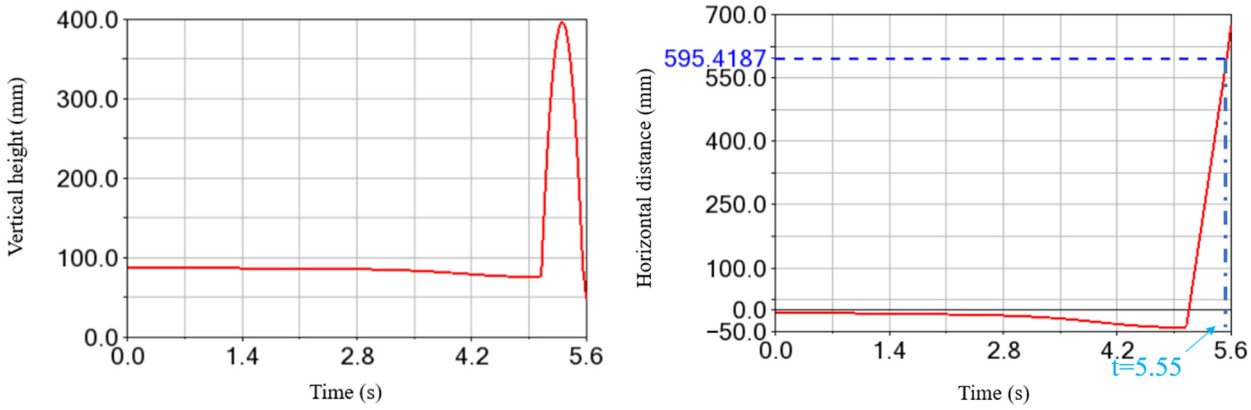

Figure 10. (**a**) Vertical height displacement of the center of mass; (**b**) Horizontal distance displacement of the center of mass.

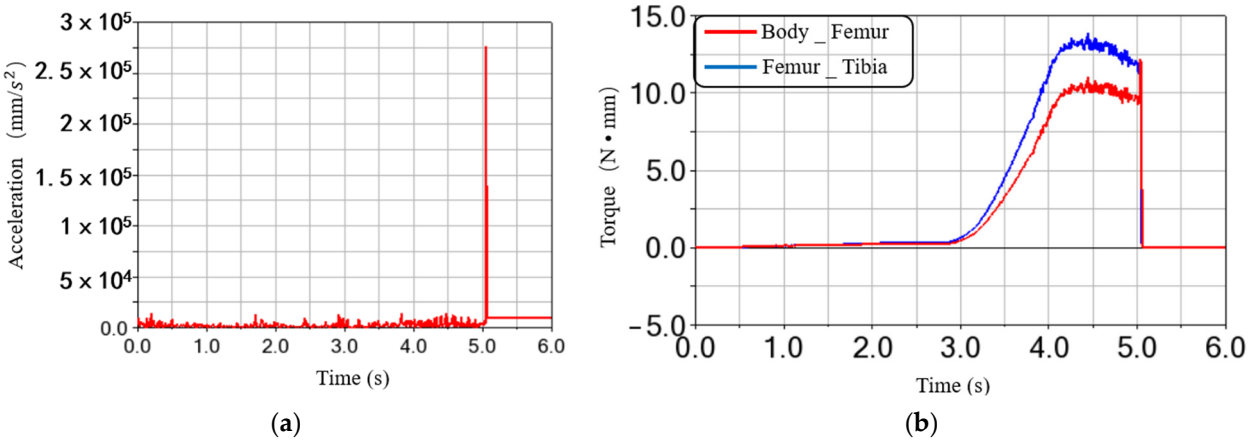

Figure 11. (**a**) Acceleration of the robot's center of mass; (**b**) Graph of torque change during the jumping phase.

5. Prototyping and Experimental Testing

To measure the actual jumping performance of the bouncing robot, experimental tests were carried out on the prototype robot. The control board was a one-way control board with a DIY wireless servo. Aluminum alloy was utilized for the six-link mechanism, the joint parts and the gear set of the energy control mechanism were made of robust nylon

fiberglass, and the rest of the components were made of resin. A high-speed camera was used to record the jumping process and to obtain the robot's attitude and position at the highest point and the landing point, as shown in Figure 12.

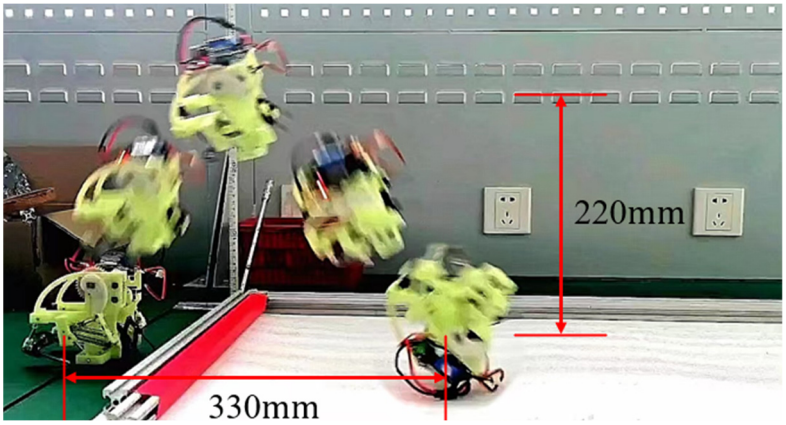

Figure 12. Robot prototype jump test.

With 600.2 mJ of energy fully released, the test results showed that the vertical height of the jumping robot was 220 mm, the horizontal distance was 330 mm, and its jumping speed was 2.21 m/s, of which the vertical speed was 2.11 m/s and the horizontal speed was 0.66 m/s. The overall energy consumption efficiency was 67%, with the majority of energy lost due to the friction of each rotating connection and air resistance during the jumping process. As the simulation cannot fully simulate the contact between the end of the robot's hind foot and the end of the forefoot and the ground, as well as the influence of realistic factors such as physical prototype production defect, there is a certain degree of discrepancy between the simulation results and the experimental results.

Many bouncing robots have a high jumping capacity, but researchers have rarely considered the impact of the bouncing robot's mass on the weight of the robot. For example, the MSU Jumper has a jump height of 872 mm and a distance of 898 mm at zero loads, but a 4 g increase in weight decreases jump performance by 5.8% and an 8 g increase in weight decreases jump performance by 20.3% (695 mm jump height and 678 mm jump distance at 8 g), which shows that the weight of the robot greatly affects its jump performance. This shows that the weight of the robot itself greatly affects its jumping performance. To better highlight the performance of the bouncing robot, this paper proposes a reference factor $\Gamma = m\left(v_x^2 + v_y^2\right)$ from the perspective of the bouncing performance of the robot per unit weight. The variable m represents the weight of the robot, the variable v_x and the variable v_y represent the horizontal and vertical velocity of the robot when it starts to jump, and it responds to the relationship between the bouncing performance of the robot and its weight. Next, the above equation can be simplified by the physics equation for oblique throwing motion as $\Gamma = m\left(4h^2 + x^2\right)/2h$, where: variable h represents the height of the robot's bounce and variable x represents the distance of the robot's bounce. Furthermore, some representative micro-robots and their characteristics are compared, as shown in Table 3 below.

The weight of the robot varies negatively with jumping performance, with larger values of Γ indicating better jumping performance. Although the introduced reference factors may not reflect the relationship between robot weight and jumping ability completely and accurately, they can reflect the robot's jumping performance per unit weight to some extent. After comparative analysis, it was found that the reference factors proposed in this paper have some reference value for measuring the bouncing ability of a robot per unit weight. Specifically, the energy storage density of the bouncing robot proposed in this paper is 600.2 mJ, and its reference factor Γ value is 11.454. Compared with existing miniature

bouncing robots, the bouncing robot in this paper has a high energy storage density and a certain advantage in bouncing performance per unit weight.

Table 3. Comparison of the characteristics of miniature bouncing robots.

Bouncing Robot	Weight (g)	Jump Height (mm)	Jumping Distance (s)	Energy Value (mJ)	Parameters Γ
GRILLO III [11]	22	100	200	31.8	0.88
Miniature jumping robot [10]	7	1380	790	154	2.09
MSU Jumper [21]	23.5	872	898	-	5.185
Mini-Whegs [22]	191	18	-	-	0.688
JelloCube [23]	250	70	180	-	9.285
This article robot	166.6	220	330	600.2	11.454

6. Conclusions

This study has presented the overall structural design of a bouncing robot with high energy density based on the jumping mechanism of the wax cicada. An optimized parametric analysis model of the six-bar mechanism was established, and the influence of two variables of the six-bar mechanism—the angle of C_1DG and the length of DG—on the spring deformation variables was ultimately proposed.

The kinetic model of the jumping phase was established, and the joint angle of the robot was obtained using kinetic equations and compared to simulation results in the ADAMS environment to verify the validity of the kinetic equations.

Simulation of the jumping performance of the robot was carried out in the ADAMS virtual prototype environment. The feasibility of the entire implementation of the jumping robot was validated by analyzing the jumping motion of the robot in one cycle, and the jumping performance in the simulation environment was obtained. The simulation results show that the bouncing robot has good jumping ability and air posture stability.

A physical prototype was assembled using 3D printing and other techniques, and experimental tests were completed. The results show that with an energy storage capacity of 600.2 mJ, the robot can overcome obstacles with a height of about 220 mm and a distance of about 330 mm and does not flip significantly in the air. Compared to existing miniature bouncing robots, the bouncing robot developed in this paper has a higher energy storage density and better bouncing performance per unit weight.

In this paper, we have designed an energy storage mechanism with a high energy density of up to 600.2 mJ based on bionic principles. This design may provide a valuable reference for future research on energy storage in footed bouncing robots. However, we are aware of some shortcomings in the design of this paper, which need further research and improvement. Future research could explore higher energy density energy storage mechanisms and add other movement modes to expand the range of applications of the robot in different environments.

Author Contributions: Conceptualization: X.B.; Data collection: X.B.; Design methodology: X.B.; Theoretical analysis: X.B.; Software: X.B.; Experiments and testing: X.B.; Writing—original draft: X.B.; Writing—review and editing: X.B., D.K., Q.W., X.Y. and X.X. All authors have read and agreed to the published version of the manuscript.

Funding: This research was supported by Plan for Anhui Major Provincial Science & Technology Project, grant number 202203a06020002.

Institutional Review Board Statement: Not applicable.

Informed Consent Statement: Not applicable.

Data Availability Statement: The data used to support the findings of this study are available from the corresponding author upon request.

Conflicts of Interest: The authors declare no conflict of interest.

References

1. Zhao, J.; Chen, Y.; Wang, J. Fractional order-based control of leg impedance in electric wheeled and footed robots. *Trans. Beijing Inst. Technol.* **2019**, *39*, 187–192.
2. Sun, J.; Sun, Z.; Xin, P. A Review on the Development of Foot Robots for Deep Space Landing Exploration. *China Mech. Eng.* **2021**, *32*, 1765–1775.
3. Wang, S.; Shi, M.; Yue, B. Research on vibration isolation control of wheel-footed robots based on adaptive impedance control. *Trans. Beijing Inst. Technol.* **2020**, *40*, 888–893.
4. Zhu, L.; Fan, J.; Zhao, J. A multi-joint tracked robot for autonomous obstacle-crossing motion planning. *J. Harbin Inst. Technol.* **2012**, *44*, 88–93.
5. Song, Y.; Zhang, Y.; Yao, Q. A path-following control method for crawler robots based on heuristic dynamic planning. *Trans. Chin. Soc. Agric. Mach.* **2019**, *50*, 24–33.
6. Yao, Y.; Wang, S.; Cheng, J. Multi-mode adaptive differential tracked robot. *J. Nanjing Univ. Aeronaut. Astronaut.* **2017**, *49*, 757–765.
7. Kaspari, M.; Weiser, M.D. The size-grain hypothesis and interspecific scaling in ants. *Funct. Ecol.* **1999**, *13*, 530–538. [CrossRef]
8. Birch, M.C.; Quinn, R.D.; Hahm, G. Design of a cricket microrobot. In Proceedings of the IEEE International Conference on Robotics and Automation, San Francisco, CA, USA, 24–28 April 2000.
9. Laksanacharoen, S.; Pollack, A.J.; Nelson, G.M. Biomechanics and simulation of cricket for microrobot design. In Proceedings of the IEEE International Conference on Robotics and Automation, San Francisco, CA, USA, 24–28 April 2000.
10. Kovac, M.; Fuchs, M.; Guignard, A. A miniature 7g jumping robot. In Proceedings of the 2008 IEEE International Conference on Robotics and Automation, Pasadena, CA, USA, 19–23 May 2008.
11. Li, F.; Liu, W.; Fu, X. Jumping like an insect: Design and dynamic optimization of a jumping mini robot based on bio-mimetic inspiration. *Mechatronics* **2012**, *22*, 167–176. [CrossRef]
12. Ye, C.; Wang, B.; Wei, B. Modeling and Analysis of a Jumping Robot with Deforming Wheeled Mechanism. In Proceedings of the 2018 IEEE International Conference on Mechatronics and Automation (ICMA), Changchun, China, 5–8 August 2018.
13. Wang, D.; Sui, F.; Qiu, W. An Untethered Crawling and Jumping Micro-Robot. In Proceedings of the 2021 21st International Conference on Solid-State Sensors, Actuators and Microsystems (Transducers), Orlando, FL, USA, 20–24 June 2021.
14. Kurniawan, R.; Fukudome, T.; Qiu, H. An Untethered 216-mg Insect-Sized Jumping Robot with Wireless Power Transmission. In Proceedings of the 2020 IEEE/RSJ International Conference on Intelligent Robots and Systems (IROS), Las Vegas, NV, USA, 24 October 2020–24 January 2021.
15. Shen, Y.; Ge, W.; Mo, X. Design of a locust-inspired miniature jumping robot. In Proceedings of the 2018 IEEE International Conference on Robotics and Biomimetics (ROBIO), Kuala Lumpur, Malaysia, 12–15 December 2018.
16. Burrows, M.; Shaw, S.R.; Sutton, G.P. Resilin and chitinous cuticle form a composite structure for energy storage in jumping by froghopper insects. *BMC Biol.* **2008**, *6*, 41. [CrossRef] [PubMed]
17. Siwanowicz, I.; Burrows, M. Three dimensional reconstruction of energy stores for jumping in planthoppers and froghoppers from confocal laser scanning microscopy. *eLife* **2017**, *6*, e23824. [CrossRef] [PubMed]
18. Bonsignori, G.; Stefanini, C.; Scarfogliero, U. The green leafhopper, Cicadella viridis (Hemiptera, Auchenorrhyncha, Cicadellidae), jumps with near-constant acceleration. *J. Exp. Biol.* **2013**, *216*, 1270–1279. [CrossRef] [PubMed]
19. Burrows, M. Energy storage and synchronisation of hind leg movements during jumping in planthopper insects (Hemiptera, Issidae). *J. Exp. Biol.* **2010**, *213*, 469–478. [CrossRef] [PubMed]
20. Sutton, G.P.; Burrows, M. Biomechanics of jumping in the flea. *J. Exp. Biol.* **2011**, *214*, 836–847. [CrossRef] [PubMed]
21. Zhao, J.; Xu, J.; Gao, B.; Xi, N.; Cintron, F.J.; Mutka, M.W.; Xiao, L. MSU jumper: A single-motor-actuated miniature steerable jumping robot. *IEEE Trans. Robot.* **2013**, *29*, 602–614. [CrossRef]
22. Lambrecht, B.G.A.; Horchler, A.D.; Quinn, R.D. A small, insect inspired robot that runs and jumps. In Proceedings of the 2005 IEEE International Conference on Robotics and Automation, Barcelona, Spain, 18–22 April 2005.
23. Li, S.; Rus, D. JelloCube: A Continuously Jumping Robot with Soft Body. *IEEE ASME Trans. Mechatron.* **2019**, *24*, 447–458. [CrossRef]